

# Autonomous Calibration of MEMS Disk Resonating Gyroscope for Improved Sensor Performance

Ian B. Flader, Chae H. Ahn, Dustin D. Gerrard, Eldwin J. Ng, Yushi Yang, Vu A. Hong, Marco Pavone, and Thomas W. Kenny

**Abstract**—This work describes a new method for autonomous mode-matching and quadrature nulling of a Microelectromechanical system (MEMS) wineglass mode gyroscope, utilizing particle swarm optimization. Use of this derivative-free optimization scheme allows for multi-objective optimization of gyroscopic performance parameters. Modal frequency split and both mode shapes' quadrature and amplitude were optimized through this method. Optimal parameters for frequency split, quadratures, and principle axis amplitudes were found to be 0.71 Hz, 13.9 and 10.5 mV, and 284.6 and 299.6 mV, respectively. Autonomous calibration greatly increased the scale factor of the sensor and enhanced the noise performance to levels typically achieved by diligent hand tuning.

## I. INTRODUCTION

### A. Inertial sensors: The push towards miniaturization

MEMS applications are becoming widespread as micro- and nano-fabrication techniques continue to push the boundaries of size, cost, and limitations for electronic devices. These devices are gaining traction in diverse fields such as biomedical [1]-[3], robotics [4]-[5], and energy [6]-[7]. Concepts such as lab-on-a-chip [8] and the internet of things [9] are driving academic interests, while the consumer electronics revolution is currently fueling the technology industry.

Inertial sensors are a subset of MEMS that transduce inertial forces into electrical signals, which are then processed by other electronic components. Miniaturized gyroscopes are one such type of inertial transducer that play an integral role in technologies such as sensor fusion [10] and dead reckoning [11]. For these reasons, MEMS gyroscopes are an area of strong academic and commercial interest.

### B. The Stanford encapsulation process

The device studied in this work was a micro-scale gyroscope fabricated using a wafer-scale encapsulation process developed at Stanford University in a collaborative effort with the Robert Bosch Corporation [12]. In this process, silicon micro devices are sealed in a cavity by depositing an epitaxial silicon encapsulation layer. The encapsulation happens in a high temperature and low

pressure environment that yields extremely clean and hermetic conditions for the devices. The Stanford process enables the fabrication of devices that have inherently low damping due to the near vacuum environment of the encapsulation [13]-[14]. The level of damping for resonators is quantified by the quality factor or Q. Variants of this process have yielded devices with quality factors over 1M [15].

### C. Disk resonating gyroscope: Principles of operation

Miniaturization of gyroscopes has been of great interest to industry and academic communities, with the disk resonating gyroscope (DRG) being a structure of particular interest. The DRG consists of a series of concentric rings that are centrally anchored to the silicon substrate [16]-[22] and attached to neighboring rings by a series of spokes. Electrodes are located circumferentially around the structure for electrostatic actuation and capacitive sensing. The DRG is typically operated as a gyroscope in its wineglass mode, which is the second order vibrational pattern of the concentric ring structure. When the structure is driven into resonance along one of the mode shapes' principle axes, an angular rotation will transduce the driven mode's energy to the secondary mode through the Coriolis force. Output of the secondary mode can then be used to determine the angular rate applied to the device. Gyroscopic operation of the wineglass mode is shown schematically in Figure 1.

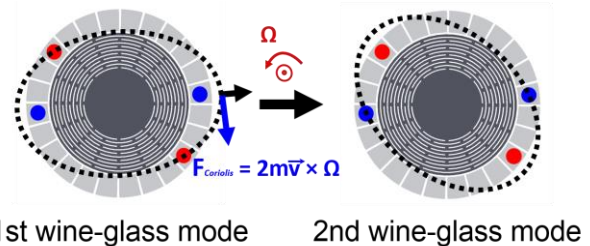


Figure 1. Diagram of wineglass mode operation for a DRG. The Coriolis force couples the two mode shapes through the velocity. Left: 0° principle axis mode. Right: 45° principle axis mode. Blue and red dots depict nodal points of each mode shape.

The wineglass mode shape of the DRG is of particular interest due to its capacity for higher sensor sensitivity, vibration rejection, and common mode noise reduction. Sensitivity of the gyroscopic structure is greatest when the eigenmodes are operated in a state of degeneracy, which is the condition where two eigenmodes maintain the same eigenfrequency. However, the wineglass mode loses degeneracy in silicon due to the anisotropy of the crystalline

I. B. Flader, C. H. Ahn, D. D. Gerrard, E. J. Ng, Y. Yang, V. A. Hong, and T. W. Kenny are with the Department of Mechanical Engineering, Stanford University, Stanford, CA 94305. {iflader, ahn1229, dustinggerrard, eldwin, ysyang88, vuhong}@stanford.edu, kenny@cdr.stanford.edu

M. Pavone is with the Department of Aeronautics & Astronautics, Stanford University, Stanford, CA 94305. pavone@stanford.edu

structure. Further, loss of degeneracy occurs in isotropic materials due to manufacturing and fabrication tolerances as well as inhomogeneity in the crystalline structure. The loss of degeneracy induces a mismatch in the resonant frequency of the two wineglass mode shapes, which results in a significant reduction in sensitivity. Despite this loss of degeneracy, it is possible to achieve near degenerate gyroscopic operation through electrostatic softening of the structure stiffness. By applying bias voltages to the circumferential electrodes, it is possible to reduce the resonant frequencies of each mode shape through a process known as electrostatic tuning [23]. It is also possible to account for a large portion of the discrepancy in the resonant frequencies through geometric design by adjusting the stiffness of each individual mode. However, precise nulling of the frequency split is not possible through this method. Therefore, the active, electrostatic calibration step previously described is critical for devices regardless of the fabrication material or geometry. This calibration step is typically done by meticulous hand tuning. However, development of autonomous calibration schemes is imperative for applications where calibrations by a technician are impossible or costly. Such applications include consumer products, aviation, aeronautics, and exploratory endeavors.

## II. TUNING MODEL FOR STRONG AND WEAK COUPLING OF TWO-LEVEL SYSTEMS

Two level systems are encountered in a wide range of fields [24]-[26]. Behavior of these systems can be observed when the energies of two systems are allowed to interact. Zener was one of the first to describe the phenomenon [27], and others have subsequently provided classical interpretations to the formulation [28]. In this section we develop the two-level model for the wineglass gyroscopic modes following the classical interpretation of Zener's coupled oscillators.

### A. Two-level representation of the disk resonating gyroscope

The wineglass mode gyroscope can be described as a two-level system with an effective mass, damping, and stiffness for each mode shape [29]. In this generalization, both mode shapes are represented by a two degree of freedom (DOF) system with independent coordinates  $x$  and  $y$ , shown in Figure 2.

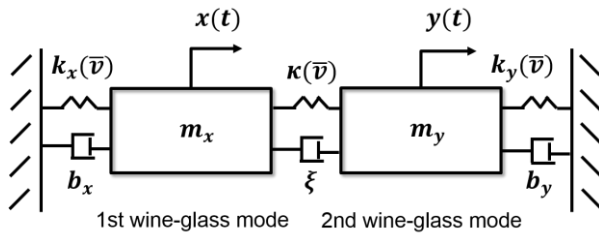


Figure 2. Lumped-element model of the DRG. Each mode is represented as one DOF with independent mass, damping, and stiffness. Internally, the structure has damping and stiffness which may couple the two modes.

Each mode shape has an independent effective mass, spring, and damper. The mode shapes are coupled by an internal spring and damper. The stiffness of each mode, as well as the coupling stiffness, were tuned using electrostatic voltages. Tuning was achieved by applying DC voltages to specific electrodes to perform electrostatic softening on the device structure. The dynamic equations for the generalized system in the presence of angular rotation are derived in Equations (1a-b), and the state-space representation is given in Equations (2a-b).

$$m_x \ddot{x} + b_x \dot{x} + k_x x = \dots \\ F_x(t) + 2A_g m_y \Omega_z \dot{y} + \xi(\dot{y} - \dot{x}) + \kappa(y - x) \quad (1a)$$

$$m_y \ddot{y} + b_y \dot{y} + k_y y = \dots \\ F_y(t) - [2A_g m_x \Omega_z \dot{x} + \xi(\dot{y} - \dot{x}) + \kappa(y - x)] \quad (1b)$$

$$\begin{bmatrix} m_x & 0 \\ 0 & m_y \end{bmatrix} \ddot{\bar{u}} + \begin{bmatrix} b_x + \xi & \xi \\ \xi & b_y + \xi \end{bmatrix} \dot{\bar{u}} + \begin{bmatrix} k_x + \kappa & \kappa \\ \kappa & k_y + \kappa \end{bmatrix} \bar{u} = \dots \\ \begin{bmatrix} F_x(t) \\ F_y(t) \end{bmatrix} + 2A_g \Omega_z(t) \begin{bmatrix} 0 & m_y \\ -m_x & 0 \end{bmatrix} \dot{\bar{u}} \quad (2a)$$

$$\bar{u} = \begin{bmatrix} x \\ y \end{bmatrix} \quad (2b)$$

The independent modal mass, damping, and stiffness are represented as  $m_{x,y}$ ,  $b_{x,y}$ , and  $k_{x,y}$ , respectively.  $\Omega_z$  is the angular rotation rate applied, and  $A_g$  is the angular gain of the structure.  $F_x$  and  $F_y$  are external excitations applied to the structure, and  $\xi$  and  $\kappa$  are the internal damping and stiffness coupling the two modes. It is important to note that each stiffness,  $k_{x,y}$  and  $\kappa$ , is a function of an applied set of DC voltages, denoted  $\bar{v}$ , shown in Figure 2. The voltage dependent stiffness is used to model the electrostatic softening effect utilized experimentally to achieve mode-matching of the wine-glass modes.

Given the dynamic equations of the system, it is possible to set up the eigenvalue problem and solve for the natural frequencies of the two mode shapes. The eigenfrequency of one mode is allowed to vary with a tuning parameter, in this case a voltage. Figure 3 shows the generalized eigenfrequencies as a function of the tuning parameter. Two regimes exist when investigating eigensolutions of two level systems. The first is the strong coupling regime where the eigenbranches approach one another, then diverge without crossing. This characteristic is known as the anti-crossing or avoided crossing. The second case is the weak coupling regime where the eigenbranches approach one another, then cross. The tuned mode does not impact the secondary mode because there is no coupling between them. The model was evaluated for the level of damping these devices typically encountered in the Stanford fabrication process ( $Q = 100k$ ) as well as the case with no damping. We determined that damping effects for this system were negligible in regard to both the strong (Figure 3 top) and weak (Figure 3 bottom) coupling regimes. Therefore, Equations (3a-f) can be used as a simplified model (ignoring damping) to obtain intuition for the mode coupling system.

$$\ddot{\mathbf{u}} = \underbrace{\begin{bmatrix} \frac{k_x + \kappa}{m_x} & -\frac{\kappa}{m_x} \\ \frac{\kappa}{m_y} & \frac{k_y + \kappa}{m_y} \end{bmatrix}}_A \mathbf{\bar{u}} \quad (3a)$$

$$|A - \omega^2 I| = 0 \quad (3b)$$

$$\omega_{\pm}^2 = \frac{1}{2} \left[ (\omega_x^2 + \omega_y^2) \pm \sqrt{(\omega_x^2 - \omega_y^2)^2 + 4\Gamma^2 \omega_x \omega_y} \right] \quad (3c)$$

$$\Gamma = \frac{\sqrt{\kappa/m_x} \sqrt{\kappa/m_y}}{\sqrt{\omega_x \omega_y}} \quad (3d)$$

$$\omega_x = \sqrt{k_x/m_x}, \quad \omega_y = \sqrt{k_y/m_y} \quad (3e-f)$$

It can be shown that  $\Gamma$  represents the strength of the mode coupling and is shown in Figures 3 and 4. When  $\Gamma$  is zero the modes are said to be degenerate, and minimal frequency split may be achieved.

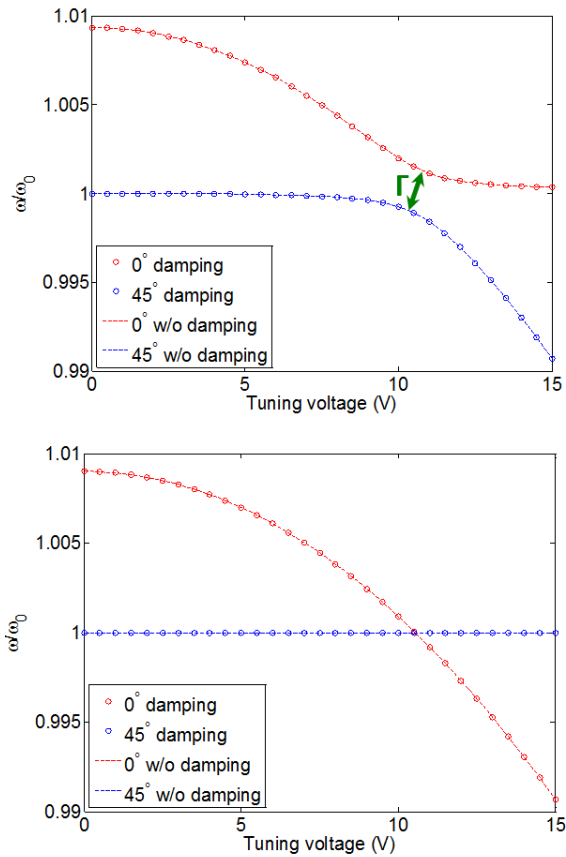


Figure 3. Simulated DRG results using the two-level model. Simulations were generated for the damped case ( $Q = 100k$ ) and the undamped case. Top: strong coupling regime where internal coupling is considered. Bottom: weak coupling regime where internal coupling is neglected.

### C. Empirical evidence of strong and weak coupling in wineglass modes

Strong coupling behavior was observed through the quality factor in [30] by measuring the quality factor of interacting, nondegenerate DRG modes. However, the frequency behavior was unable to be resolved due to improper electrode alignment to the desired mode shapes. In this work, strong coupling was investigated in the wineglass modes by measuring the resonant frequency of each mode shape using two drive and sense pairs (D1-S1, D2-S2). A bias voltage,  $T_A$ , was applied to the S2 electrode position to electrostatically soften the higher frequency mode, shown in Figure 4 (top). Figure 4 (top) shows that with no other electrostatic forces, the wineglass modes are misaligned and operate in the strong coupling regime. This is poor for device performance, as the strength of the coupling prevents adequate mode-matching. However, by applying bias voltages to the electrodes that do not align (off principle axis, or off axis, electrodes) with the wineglass principle axes, it is possible to nullify the mode coupling by realigning the vibration pattern to the fixed electrodes, shown in Figure 4 (bottom).

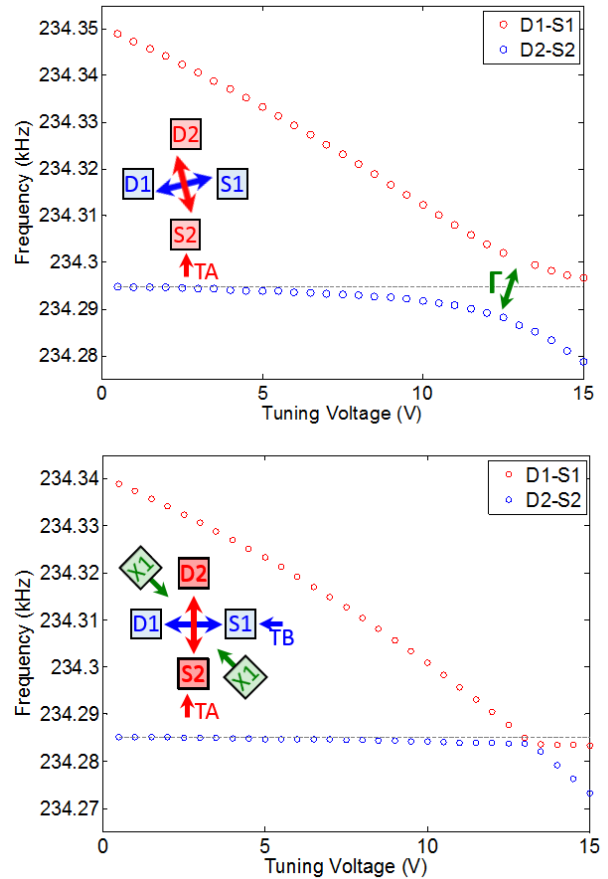


Figure 4. Experimental DRG results revealing the two-level system behavior. (Top) Without appropriate cross tuning to realign the vibration pattern, the strong coupling regime can be observed. (Bottom) With appropriate cross tuning, the weak coupling regime can be observed with near degenerate conditions.

The misalignment of the wineglass mode vibration patterns induces quadrature output of each mode. Quadrature is the

measure of output from one wineglass mode when the other mode is driven. Since the two modes are orthogonal, the output of a mode when the other is driven should be null. However, the misalignment couples the two systems and produces a quadrature signal. The bias voltage used for realigning the mode shapes is known as the cross tuning voltage and can be applied to the  $22.5^\circ$  (X1) or  $67.5^\circ$  (X2) electrode locations. Figure 5 shows experimentally that for various values of cross tuning, the coupling can be decreased to allow for adequate mode-matching. However, if too much voltage is applied, the coupling begins to increase again. Therefore, a condition exists where precise values for the tuning voltages along each principle axis,  $T_A$  and  $T_B$ , and the cross tuning,  $X_1$  or  $X_2$ , yield minimal quadrature and frequency split for the two wineglass modes of the gyroscope. Determining these values is typically done with meticulous hand tuning.

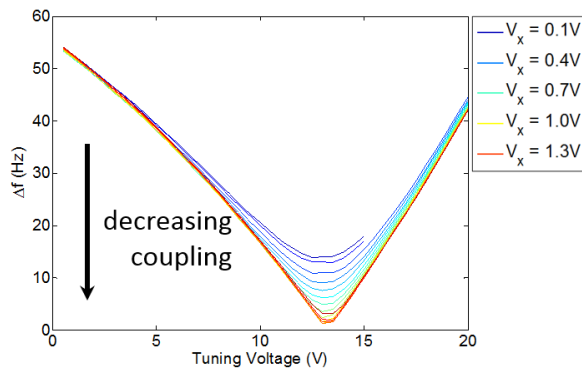


Figure 5. Resonant frequency split between the two wineglass mode shapes for various amounts of cross tuning applied.

In this section, a model was proposed for the DRG as a two-level system that captures the quadrature and frequency split relationship. It is possible with finite element analysis (FEA) to estimate the effective properties of the lumped-element model. However, despite showing that reasonable assumptions may be made to simplify the system, determination of the coupling factors is less straightforward. The sections below detail a stochastic method for autonomously calibrating the gyroscope for high sensitivity operation to circumvent this. It is important, however, to understand the underlying dynamics to create a robust calibration method. The method proposed is indifferent to the device geometry, fabrication material, and manufacturing and fabrication tolerances that provide a robust path to autonomous calibration for a multitude of device structures.

### III. CONTROL STRUCTURE

A derivative free optimization (DFO) scheme was developed to perform the autonomous calibration. Our method was derived from the particle swarm optimization (PSO) algorithm [31]. The optimizer stochastically determined the control voltage outputs to apply to the gyroscope structure to nullify the quadrature and frequency split, while maximizing the output amplitude of the independent mode shapes.

#### A. Control objective

An objective cost was defined for the resonant frequency split,  $\Delta f_r$ ; quadratures of each mode shape,  $q_1$  and  $q_2$ ; and the amplitude of each mode shape,  $A_1$  and  $A_2$ . Equation (4a) shows the objective of choice, with the weightings  $\rho$ ,  $\gamma$ , and  $\varphi$  representing the penalties on resonant frequency split, quadrature-to-amplitude ratio, and quadrature-to-amplitude ratio difference, respectively. Equation (4a) states that we wish to minimize this objective subject to the constraints that our control voltages must be within the defined boundaries. To incorporate the boundary constraints to our algorithm, we introduce an exponential barrier function,  $\theta$ , to the objective (Equation (4b)). Equation (4c) and Figure 6 show the barrier function for  $\pm 20V$ . Our control voltages are limited to this range by our lab voltage supplies.

$$\text{minimize } \rho \Delta f_r + \gamma \left( \frac{q_1}{A_2} + \frac{q_2}{A_1} \right) + \varphi \left| \frac{q_1}{A_2} - \frac{q_2}{A_1} \right| \quad (4a)$$

$$\text{subject to } \bar{v}_{min} \leq \bar{v} \leq \bar{v}_{max}$$

$$\text{minimize } \rho \Delta f_r + \gamma \left( \frac{q_1}{A_2} + \frac{q_2}{A_1} \right) + \varphi \left| \frac{q_1}{A_2} - \frac{q_2}{A_1} \right| + \theta \quad (4b)$$

$$\theta = \sum_i (e^{|v_{i,max}-v_i|^{-1}} + e^{|v_{i,min}-v_i|^{-1}}) \quad (4c)$$

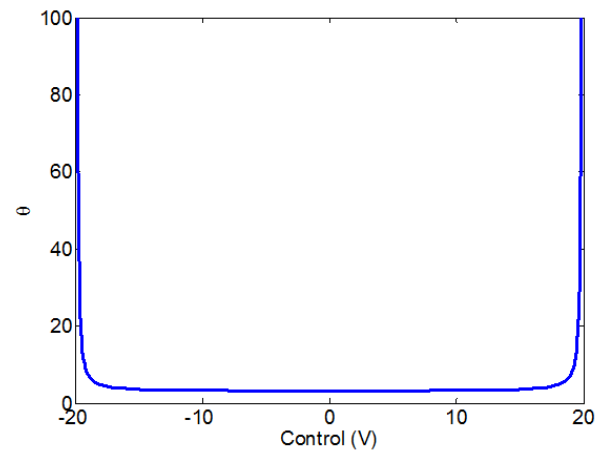


Figure 6. Exponential barrier function over the permissible voltage range.

#### B. Control formulation

The problem described above can be represented by a simple input-output regulatory control model as in Figure 7.

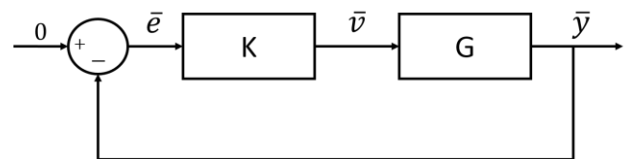


Figure 7. Input-output regulatory control representation of the quadrature and frequency split nulling problem. The plant,  $G$ , is a black box with measurable outputs,  $\bar{y}$ . The controller,  $K$ , is a digital, stochastic controller with dynamics described by Equations (6a-b).

In this case, we treat our plant,  $G$ , as a black box, which can provide measurements of the system. The digital controller,  $K$ , is the PSO variant described in the section above. The plant takes input as a vector of voltages in  $\mathbb{R}^3$  and outputs the parameters of interest in  $\mathbb{R}^5$  as shown in Equations (5a-b). The dynamics of the controller are described by Equations (6a-b), where  $d$  and  $v$  represent the pseudo-position and pseudo-velocity of the particles.

$$\bar{v} = \begin{bmatrix} T_A \\ T_B \\ X_2 \end{bmatrix}, \quad \bar{y} = \begin{bmatrix} \Delta f_r(\bar{v}) \\ q_1(\bar{v}) \\ q_2(\bar{v}) \\ A_1^{-1}(\bar{v}) \\ A_2^{-1}(\bar{v}) \end{bmatrix} \quad (5a-b)$$

$$\bar{d}_i^{n+1} = w\bar{d}_i^n + c_1r_1^n(\bar{p}_i^n - \bar{v}_i^n) + c_2r_2^n(\bar{g}^n - \bar{v}_i^n) \quad (6a)$$

$$\bar{v}_i^{n+1} = \bar{v}_i^n + \bar{d}_i^{n+1} \quad (6b)$$

In this case, these translate to the control voltages and their rates of change. The up-to-date local minima and global minima, as determined by the particles of the current iteration, are represented as  $p$  and  $g$ , respectively. The weighting of the controller dynamics is represented by  $w$ ,  $c_1$ , and  $c_2$ .  $r_1$  and  $r_2$  represent the uniformly distributed random values that encourage the random walk behavior of the controller. The iteration and particle numbers are represented by  $n$  and  $i$ , respectively.

### C. Control algorithm

The stochastic control algorithm was implemented following the process shown in Figure 8. The specifics of each step may be found in the appendix.

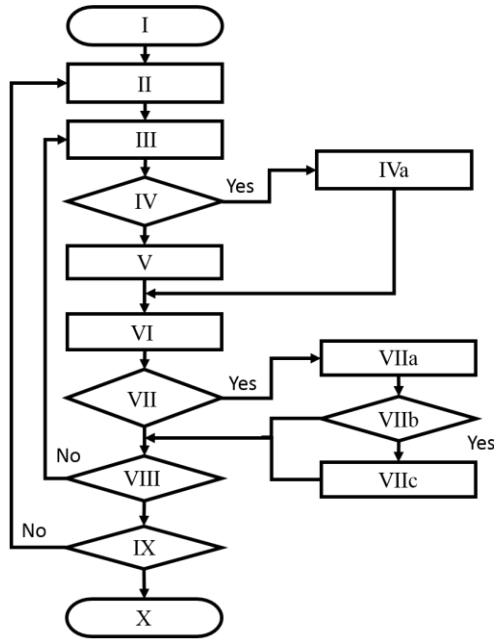


Figure 8. Particle swarm optimization process for application of quadrature nulling and mode-matching of the wineglass mode shapes for the DRG.

The control algorithm consists of multiple particles, or probes, of the plant. Each particle is a vector of control voltages, which are aware of the associated objective costs for applied controls from previous iterations as well as the associated objective costs from other particles. Particles are updated as prescribed by Equations (6a-b) given the contextual information of the plant. This is done in an iterative fashion until the plant is optimized.

Multiple re-initializations are performed to ensure that minimal solutions are obtained instead of asymptotic approaches to local optimums. This was done by initializing particles in a confined window once asymptotic behavior was achieved. In this way, regions of fine resolution were probed near local optimums once steady state operation had been reached.

## IV. EXPERIMENTAL RESULTS

### A. Device design

The device in this study was a  $60\mu\text{m}$  thick  $\langle 100 \rangle$  single crystal silicon (SCS) DRG with ring widths varied to passively tune the geometry for better mode-matching [23]. The design was successful in greatly reducing the fabricated resonant frequency split from the symmetric case in  $\langle 100 \rangle$  SCS; however, electrostatic tuning was required for fine tuning the gyroscope for high sensitivity performance. The algorithm was also tested on various other materials and geometries, and is discussed in §IV-D

### B. Experimental setup

The control procedure detailed in the previous section was utilized to autonomously nullify the resonant frequency split and modal quadratures. The device was wired electrically as provided by the schematic in Figure 9. The two mode shapes were driven into resonance with a  $20\text{ mV}_{\text{ac}}$  closed-loop excitation, independently, while the necessary measurements were made as prescribed by the control law. The measurements were then fed to the optimizing algorithm to determine the next iterative step in applied control voltages.

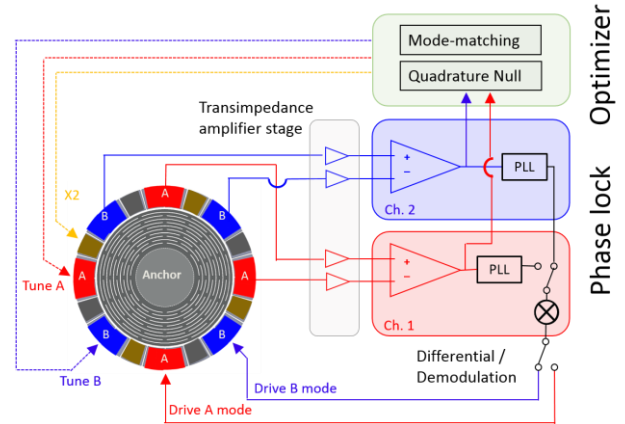


Figure 9. Experimental setup schematic for the quadrature nulling and mode-matching. Two channels of a phase locking system were used to obtain measurements that were fed to the optimizer. The optimizer determines the control voltages ( $T_A$ ,  $T_B$ ,  $X_2$ ) to apply to the structure.

### C. Results

The multi-objective optimization of the DRG for resonant frequency split, quadratures, and amplitudes was successful in achieving values of 0.71 Hz, 13.9 and 10.5 mV, and 284.6 and 299.6 mV, respectively. Figure 10 shows the results of the optimization for the objective parameters.

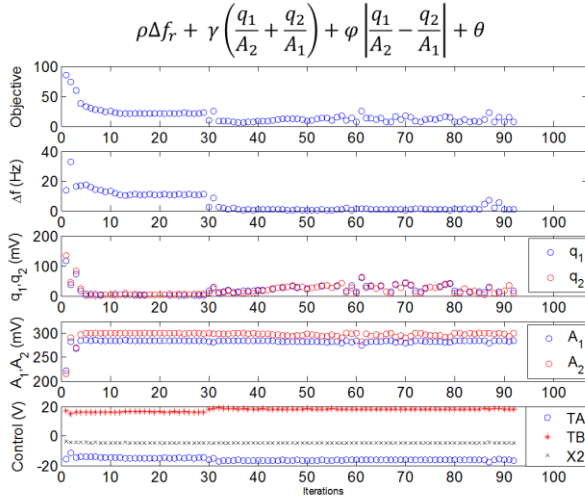


Figure 10. PSO objective outputs over the specified iterations. The optimizer minimizes the objective by determining control voltages to provide minimal frequency split and quadrature, while maximizing modal amplitudes.

Optimizing the quadrature, amplitude, and frequency split enhances the device performance by increasing the scale factor and decreasing the Allan deviation. The scale factor is the transfer function which determines the electronic output for a given angular rate input, and the Allan deviation is a measure of the noise in the physical sensor. Figure 11 shows the scale factor output from the gyroscope when subjected to  $10^0/s$  rotation input rate.

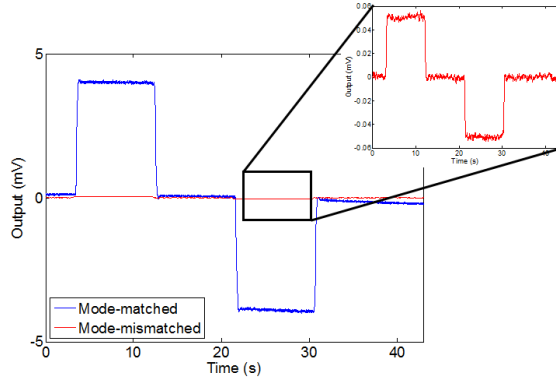


Figure 11. Sensor output from the gyroscope when subjected to a  $10^0/s$  input angular rate for both mode-matched and mode-mismatched operation. Sensor output becomes much higher for near degenerate operation. Inset: magnification of mode-mismatched signal over the full time span.

The scale factor increased from  $5 \mu V/0/s$  for the as fabricated device to  $401 \mu V/0/s$  after the autonomous calibration. The noise performance was also measured by determining the Allan deviation. Figure 12 shows that the angular random walk decreased from 0.51 to  $8.8e-3^0/s/\sqrt{Hz}$  and the bias instability decreased from 0.036 to  $7.7e-3^0/s$ . These values are comparable to expert hand tuning [32].

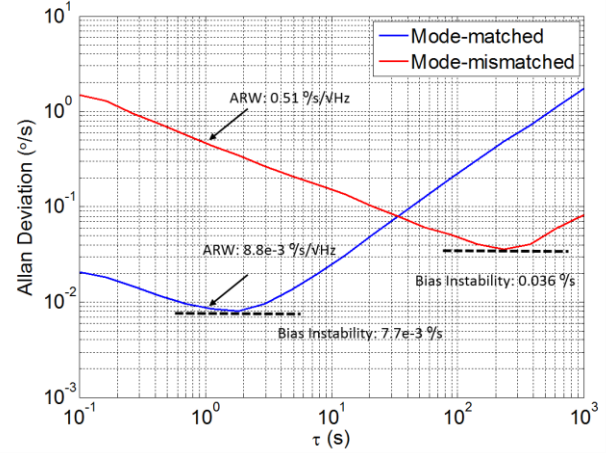


Figure 12. Allan deviation over the integration time,  $\tau$ . Angle random walk (ARW) and bias instability were much improved by operating near degeneracy.

### D. Autonomous calibration of various gyroscope designs

Due to the stochastic nature of the optimization scheme, it was possible to optimize various gyroscope geometries made of differing materials. Table 1 shows the summarization of results for two gyroscopes fabricated from  $\langle 100 \rangle$  SCS material, one fabricated from  $\langle 111 \rangle$  SCS, and another fabricated from polycrystalline silicon (P-Si). The width varying device is the structure described in detail in §IV-A of this paper. The  $\langle 100 \rangle$  spoke angle variation device was a  $40\mu m$  thick DRG where the angles of the connecting spoke beams were adjusted to passively tune to resonant frequencies of the wineglass mode shapes. The  $\langle 111 \rangle$  and P-Si devices were fabricated in the  $\langle 111 \rangle$  SCS and polycrystalline silicon isotropic materials, respectively. These DRGs were  $40\mu m$  and  $20\mu m$  thick, respectively, and had a symmetric design with no passive compensation. The stochastic optimizer provided robust optimization that was capable of autonomously calibrating gyroscopes regardless of their geometric and material configuration, and yielded significant performance improvement for all devices. The performance of these gyroscopes are detailed in [33].

TABLE I. SUMMARY OF GYROSCOPE PERFORMANCE

Device	Scale Factor ( $\mu V/0/s$ )		ARW ( $0/s/\sqrt{Hz}$ )	
	Mode-mismatched	Mode-matched	Mode-mismatched	Mode-matched
$\langle 100 \rangle$ width varying	5.05	401	0.507	$8.8e-3$
$\langle 100 \rangle$ spoke angle	1.48	146	2.27	$18e-3$
$\langle 111 \rangle$	1.94	222	0.435	$12e-3$
P-Si	4.53	73.7	0.231	$38e-3$

### V. CONCLUSION

Gyroscope calibration for high sensitivity performance requires optimization of multiple objectives. A model was

presented that captures the strong coupling behavior observed in the devices. While this model provides valuable intuition, use of the model for control purposes would have strong sensitivity to manufacturing and fabrication tolerances. Further, this paradigm would require evaluation of the effective properties for mass and stiffness for each mode shape, as well as the internal coupling between the two. A stochastic method was proposed to circumvent these concerns. The autonomous calibrator was capable of correcting the misalignment and frequency split of the two wineglass modes of the gyroscope. It was also shown that various DRG structures made from different fabrication materials could be optimized through the use of the stochastic approach.

#### APPENDIX

The following describes the logical process of the algorithm at each step:

- I. Initialization. Set the number of particles, weights, and control boundaries and windows.
- II. Generate randomized control voltages,  $v_i$ , within control windows and evaluate objective cost from Equation (4b)
 
$$\bar{g}^n = \min_i f(\bar{v}_i^n)$$

$$\bar{p}_i^n = \bar{v}_i^n$$
- III. Calculate rate of voltage change,  $d_i$ , and updated control voltages,  $v_i$ , using Equation (6a-b)
- IV. Is applied control voltage outside boundary constraint?
- IVa. Apply boundary voltage as the control voltage
- V. Apply calculated control voltage
- VI. Measure the objective parameters  $\Delta f_r$ ,  $q_1$ ,  $q_2$ ,  $A_1$ , and  $A_2$ . Evaluate the objective cost from Equation (4b).
- VII. Is the evaluated objective cost less than the current minimum for that particle?
  - VIIa. Update local minimum for that particle
 
$$\bar{p}_i^n = \bar{v}_i^n$$
  - VIIb. Is the evaluation less than the current minimum for all particles?
  - VIIc. Update minimum for all particles
 
$$\bar{g}^n = \bar{v}_i^n$$
- VIII. Iteration or tolerance criteria met for particles?
- IX. Iteration or tolerance criteria met for initializations?
- X. Objective optimized

#### ACKNOWLEDGMENT

This work was supported by DARPA grant N66001-12-1-4260, "Precision Navigation and Timing program (PNT)," managed by Dr. Robert Lutwak. The fabrication work was performed at the Stanford Nanofabrication Facility (SNF) which was supported by National Science Foundation through the NNIN under Grant ECS-9731293.

#### REFERENCES

- [1] A. Nisar, Nitin Afzulpurkar, Banchong Mahaisavariya, Adisorn Tuantranont. "MEMS-based Micropumps in Drug Delivery and Biomedical Applications." *Sensors and Actuators B: Chemical* Volume 130, Issue 2, 28 March 2008, Pages 917–942
- [2] P. Miao, P. D. Mitcheson, A. S. Holme, E. M. Yeatman, T. C. Green, B. H. Stark, "Mems Inertial Power Generators for Biomedical Applications," *Microsyst Technol* (2006) 12: 1079–1083
- [3] Amy C. Richards Grayson, Rebecca S. Shawgo, Audrey M. Johnson, Nolan T. Flynn, Yawen Li, Michael J. Cima, And Robert Langer, "A BioMEMS Review: MEMS Technology for Physiologically Integrated Devices," *Proceedings of the IEEE*, Volume:92, Issue: 1.
- [4] S. Sastry, M. Cohn, F. Tendick, "Milli-robotics for Remote, Minimally Invasive Surgery," *Robotics and Autonomous Systems* 21 (1997) 305-316.
- [5] J.R.Bronson, J. S. Pulskamp, R.G. Polcawich, C.M. Kroninger, and E.D. Wetzel, "PZT MEMS Actuated Flapping Wings for Insect-Inspired Robotics," *IEEE 22nd International Conference on Micro Electro Mechanical Systems*, 2009.
- [6] Salem Saadon, Othman Sidek, "A Review of Vibration-based MEMS Piezoelectric Energy Harvesters," *Energy Conversion and Management* 52 (2011) 500–504.
- [7] Chung-Yang Sue, Nan-Chyuan Tsai, "Human Powered MEMS-based Energy Harvest Devices," *Applied Energy* 93 (2012) 390–403. Yorozu, M. Hirano, K. Oka, and Y. Tagawa, "Electron Spectroscopy Studies on Magneto-optical Media and Plastic Substrate Interfaces," *IEEE Transl. J. Magn.Jpn.*, vol. 2, Aug. 1987, pp. 740–741.
- [8] Vijay Srinivasan, Vamsee K. Pamula, and Richard B. Fair, "An Integrated Digital Microfluidic Lab-on-a-chip for Clinical Diagnostics on Human Physiological Fluids," *Lab Chip*, 2004, 4, 310-315.
- [9] Kortuem, G.; Univ. of Lancaster, Lancaster, UK; Kawsar, F.; Fitton, D.; Sundramoorthy, V., "Smart Objects as Building Blocks for the Internet of Things," *Internet Computing*, IEEE (Volume:14, Issue: 1).
- [10] Stephane Beauregard and Harald Haas, "Pedestrian Dead Reckoning: A Basis for Personal Positioning," *Proceedings of the 3rd Workshop on Positioning, Navigation, and Communication (WPNC'06)*.
- [11] S. P. Bingulac, "On the Compatibility of Adaptive Controllers," in *Proc. 4th Annu. Allerton Conf. Circuits and Systems Theory*, New York, 1994, pp. 8–16.
- [12] R. N. Candler, W.-T. Park, H. Li, G. Yama, A. Partridge, M. Lutz, and T. W. Kenny, "Single Wafer Encapsulation of MEMS Devices," *IEEE Transactions on Advanced Packaging*, vol. 26, pp. 227- 232, 2003.
- [13] Bongsang Kim, Rob N. Candler, Renata Melamud, Matthew A. Hopcroft, Shingo Yoneoka, Hyung Kyu Lee, Manu Agarwal, Saurabh A. Chandorkar, Gary Yama, and Thomas W. Kenny "Hermeticity and Diffusion Investigation in Polysilicon Film Encapsulation for Microelectromechanical Systems." *Journal of Applied Physics* 105, 013514 (2009);
- [14] Rob N. Candler, Woo-Tae Park, Matt Hopcroft, Bongsang Kim, Thomas W. Kenny. "Hydrogen Diffusion and Pressure Control of Encapsulated MEMS Resonators." *Solid-State Sensors, Actuators and Microsystems*, 2005. *Digest of Technical Papers. TRANSDUCERS'05*.
- [15] Eldwin J. Ng, Yushi Yang, Yunhan Chen, and Thomas W. Kenny, "An Etch Hole-free Process for Temperature-compensated, High Q, Encapsulated Resonators," *Solid-State Sensors, Actuators, and Microsystems Workshop*, Hilton Head 2014, pp. 99-100, Jun 2014.

- [16] K. V. Schleglov and A. D. Challoner, "Isolated Planar Gyroscope with Internal Radial Sensing and Actuation," U.S. Patent 7,040,163, May 9 2006.
- [17] N. Yazdi, F. Ayazi, and K. Najafi, "Micromachined Inertial Sensors," *Proc. IEEE*, vol. 86, no. 8, pp. 1640–1659, Aug. 1998.
- [18] A. M. Shkel, "Type I and type II Micromachined Vibratory Gyroscopes," in *Proc. IEEE/ION Posit., Location, Navigat. Symp.*, Apr. 2006, pp. 586–593.
- [19] A. M. Shkel, "Microtechnology Comes of Age," *GPS World*, vol. 22, no. 9, pp. 43–50, Sep. 2011.
- [20] H. Johari and F. Ayazi, "High-frequency Capacitive Disk Gyroscopes in (100) and (111) Silicon," 2007 IEEE 20th International Conference on Micro Electro Mechanical Systems (MEMS), 2007, pp. 47–50.
- [21] D. Senkal, et. al., "100K Q-factor Toroidal Ring Gyroscope Implemented in Wafer-level Epitaxial Silicon Encapsulation Process," 2014 IEEE 27th International Conference on Micro Electro Mechanical Systems (MEMS).
- [22] A. D. Challoner, H. H. Ge, and J. Y. Liu, "Boeing Disc Resonator Gyroscope," Position Location and Navigation Symposium (PLANS), 2014 IEEE/ION, pp. 504–514, 2014.R.
- [23] C. H. Ahn et al., "Mode-Matching of Wineglass Mode Disk Resonator Gyroscope in (100) Single Crystal Silicon," *Journal of Microelectromechanical Systems*, vol. 24, no. 2, April 2015.
- [24] J. Charmet, et. al, "Observations of Modal Interaction in Lateral Bulk Acoustic Resonators," *Appl. Phys. Lett.*, vol. 105, no. 1, p. 013502, Jul. 2014.
- [25] M. Benyoucef et. al, "Quality-factor Enhancement of Optical Modes Mediated by Strong Coupling in Micron-size Semiconductor Disks," *Phys. Status Solidi B* 249, No. 5, pp. 925-928, 2012.
- [26] C. Wittig, "The Landau-Zener Formula." *Journal of Physical Chemistry B* 2005, 109, 8428-8430
- [27] C. Zener, "Non-Adiabatic Crossing of Energy Levels," *Proceedings of the Royal Society of London. Series A, Containing Papers of a Mathematical and Physical Character* Vol. 137, No. 833 (Sep. 1, 1932), pp. 696-702
- [28] Lukas Novotny, "Strong Coupling, Energy Splitting, and Level Crossings: A Classical Perspective," *American Journal of Physics* 78, 1199 (2010).
- [29] Cho, J.Y. (2012). High-performance Micromachined Vibratory Rate- and Rate-integrating gyroscopes. (Doctoral dissertation).
- [30] I. B. Flader, C. H. Ahn, Y. Yang, E. J. Ng, V. A. Hong, J. Baek, and T. W. Kenny, "Tunable Quality Factor through 1:1 Modal Coupling in a Disk Resonator," 2015 IEEE Sensors.
- [31] James Kennedy, "Particle Swarm Optimization," *Encyclopedia of Machine Learning*, pp 760-766.
- [32] S. Nitzan, C. H. Ahn, T.H. Su, M. Li, E.J. Ng, S. Wang, Z.M. Yang, G. O'Brien, B.E. Boser, T.W. Kenny, D.A. Horsley, "Epitaxially-encapsulated Polysilicon Disk Resonator Gyroscope," 2013 IEEE 26th International Conference on Micro Electro Mechanical Systems (MEMS).
- [33] I. B. Flader, C. H. Ahn, E. J. Ng, Y. Yang, V. A. Hong, and T. W. Kenny, "Stochastic Method for Disk Resonating Gyroscope Mode Matching and Quadrature Nulling," 2016 IEEE 29th International Conference on Micro Electro Mechanical Systems (MEMS).